The ability to take daily PET images with a high statistical accuracy while the patient remains in the proton irradiation room is a large advantage. Besides, availability of a cone beam (CB) CT system or CT apparatus in the irradiation room can offer the possibility of daily and in situ monitoring of the patient's anatomy. A prototype beam ON-LINE PET system (BOLPs) was previously constructed for basic research (10), and verification of the proton-irradiated volume in a patient's body was confirmed using a PET apparatus and a PET-CT apparatus (beam OFF-LINE PET system) (13).

A BOLPs mounted on a rotating gantry port (BOLPs-RGp) was constructed in our proton treatment room. Activity measurement and PET imaging were performed in 48 patients with tumors of the head and neck, liver, lungs, prostate, and brain during proton treatment at our facility. The position and intensity of the activity were measured daily using the BOLPs-RGp immediately after proton irradiation. Using the activity measurement, we were able to confirm whether the proton beam irradiation of the tumor was reproducibly performed during the treatment period. Moreover, changes in the activity distribution were observed as the volume of the tumor changed, and these changes were related to the delivery dose, changes in the body shape and position of the patient, and the physiologic changes. The PET images from the BOLPs-RGp were sufficient to provide high-quality proton treatment.

METHODS AND MATERIALS

Design of a beam ON-LINE PET system mounted on an RGp

Via the detection of pairs of annihilation gamma rays emitted from the generated radioactive nuclei of a patient's body, the BOLPs-RGp is designed to determine the position and activity of the positron-emitting nuclei generated in patients by proton irradiation. Figure 1 is a picture of the BOLPs-RGp. The BOLPs-RGp was developed as a standardized system for use with proton therapy devices. During proton therapy, the detector heads have many degrees of freedom and the system allows remote control adaptation to each new proton beam condition and a patient's position. As a result, the measurement of the activity distribution is simple.

A planar positron imaging system (Hamamatsu Photonics K. K., Hamamatsu, Japan) (17) was newly arranged for the BOLPs-RGp. In comparison to the system used previously (10), the 24 detector units mounted on each detector head were increased to 36 detector units, and each unit was composed of 11 × 10 arrays of BGO ($Bi_4Ge_3O_{12}$) crystals with a crystal size of 2 × 2 × 20 mm^3. Furthermore, the 2,400 crystals were increased to 3,600 crystals. The gap of each unit became 3.3 mm from 11.0 mm for minimizing dead space in the detector. The field of view (FOV) became 164.8 × 167.0 mm^2 from 120.8 × 186.8 mm^2. The maximum field size is 185.0 × 185.0 mm^2 in the rotating gantry port with the BOLPs-RGp. Therefore, the FOV can almost cover each treatment site of the head and neck, liver, lungs, prostate, and brain for a proton treatment in our facility. However, in case of prostate, the depth activity distribution is not measured in the entrance of the incident proton beam. The BOLPs-RGp was mounted on and the center of its detection area was aligned with the iso-center of the rotating gantry in the treatment room of the proton therapy facility at our center. A PET image reconstructed by a back-projection method

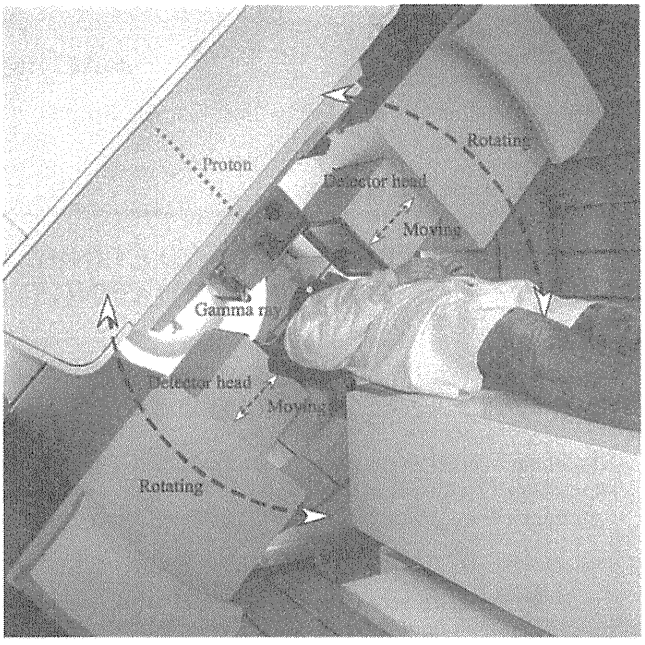

Fig. 1. Setup of the BOLPs-RGp, which is mounted on the rotating gantry port of our proton treatment room.

along the axis of the proton beam direction is always included in the FOV of the opposing detectors together with the axis of the rotating angle of the gantry system. The distance between the two opposing detector heads of the BOLPs-RGp can be adjusted from 30 to 100 cm. When the activity is not being measured, the detector head is stored inside the wall of the gantry device. The position resolution of this system is about 2 mm for the full width at half maximum in the case of use of ^{22}Na point source. The maximum data collection rate for the coincident detection of pair annihilation gamma rays is about 4,000 counts/s/cm^2 (kcps/cm^2). The accuracy of the measurements of activity distribution by this system was verified by a prototype beam ON-LINE PET system (10). The measured data are stored using in the software's list mode format. The activity image is renewed every second. The information of the on-off time points of beam irradiation is recorded in the data, and the image can be restructured according to this information. The PET data from the irradiation field of each patient are managed throughout each treatment day.

The detection efficiency of the distance between the detector heads was calibrated by using the thin-flat acrylic container filled with ^{18}F-solution. The calibration is used for a correction of the imaging uniformity and the detection sensitivity. The attenuation coefficient of 511-keV gamma rays in the patient's body was calculated by the patient's CT image data. They are used for a construction of the activity imaging. The correction of the photon scattering in the patient's body is not considered for the activity imaging. Furthermore, the photons scattered in the patient's body outside the FOV are detected by the effect of the geometry of the detector head. Therefore, the activity image is contaminated by about 10% background in this system. As the result, the position resolution of the activity distribution will become large more than 2 mm in the clinical case of a proton therapy.

Activity measurement in a patient during proton treatment

The measurement of activity was performed daily in 48 cases involving tumors of the head and neck, liver, lungs, prostate, and brain

using the BOLPs-RGp. The position and intensity of activity were measured during the 200 s immediately after proton irradiation using the trigger signal of the beam-off time. The measurement was performed using the shortest possible distance between the two opposing detector heads of the BOLPs-RGp for each patient. The average distance of the detector heads was 40 cm for the head and neck and the brain, 70 cm for the liver and the lungs, and 50 cm for the prostate. The time of 200 s after proton beam irradiation was chosen according to the intensity of activity estimated from the results of other studies (10, 13). The activity data obtained during proton irradiation were not used for PET imaging. Various types of background radiation (X-rays, gamma rays, and neutrons) occur during proton beam irradiation, and the quality of the activity image becomes markedly worse in their presence (2, 10, 15, 16). Furthermore, high radiation decreases the accuracy of the detector.

Verification of activity measurement was performed in 18, 4, 15, 10, and 1 cases involving tumors of the head and neck, the liver, the lungs, the prostate, and the brain, respectively. The typical fractional dose is 2.5 Gy equivalents (GyE = Gy × the relative biologic effectiveness: [= 1.1 = constant]) for the head and neck, 3.8 GyE for the liver, 4.0 GyE for the lungs, 2.0 GyE for the prostate, and 2.5 GyE for the brain in our facility. The irradiated field is typically planned with three fields in the head and neck and two fields in other sites. Furthermore, the typical number of irradiated field per fractional dose is one in the head and neck, liver, and prostate, and two in the lungs. The fractional dose was delivered over an irradiation time of 10–300 s. The proton beam irradiation was synchronized with the organ motion caused by respiration in the liver and the lungs.

Procedure for clinical use of activity image

A flow chart of procedure for clinical use of the BOLPs-RGp is shown in Fig. 2. In the clinical use, the main operation is to take an activity image every day and compare the activity image of the first day of treatment with each activity image during the comparatively long period of the treatment. If the difference of both the images is confirmed by reducing of the tumor size and changing of the body shape, then the new dose distribution is obtained from redose calculation of the plan on a new CT image acquisition, and the first proton treatment plan is immediately corrected to the new plan. As a result, proton treatments of high accuracy can be offered to the patient by keeping of the planned dose delivery.

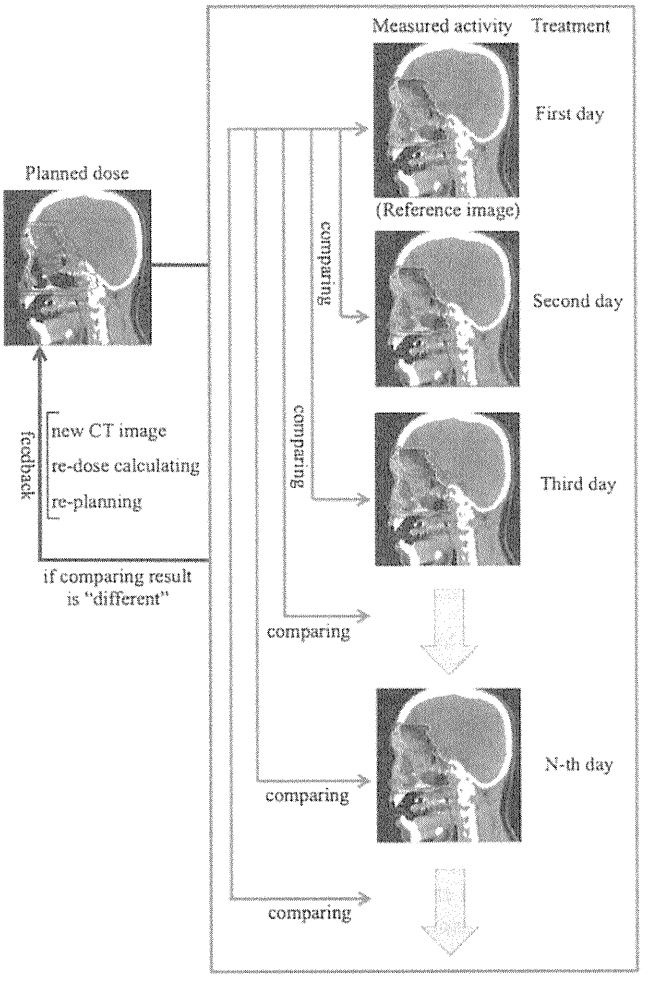

Fig. 2. Flow diagram of the procedure for the clinical use of the BOLPs-RGp.

RESULTS

Estimation of the measurement time for PET imaging

An estimation of an appropriate measurement time for PET imaging was performed using the measured activity data from tumors of the head and neck. The proton beam conditions were as follows: an energy of 120 MeV, a spread out of Bragg peak (SOBP) of 80-mm width, a gantry angle of 340°, a fractional dose of 2.5 GyE, and an irradiation time of 24 s. The distance between the detector heads was 70 cm, and the detection rate of the activity was 1.5 kcps. The left panel of Fig. 3 shows the number of detection events per volume during the detection period after proton beam irradiation. The statistical error (= standard deviation/mean value) decreased as the detection time increased. The error was 2.8% for a 200-s detection time, 3.0% for 150 s, 3.4% for 100 s, and 4.4% for 50 s. The right panel of Fig. 3 shows PET images taken using detection times of (a) 0, (b) 50, (c) 100, and (d) 200 s.

PET images of each treatment site

Typical PET images obtained by the BOLPs-RGp are shown for each case involving tumors of the head and neck, the liver, the lungs, the prostate, and the brain. Figure 4 shows the calculated dose distribution and the measured activity distribution on the first treatment day. The beam irradiation parameters were shown in Table 1. The PET images were obtained during the 200 s after proton beam irradiation. The mean detection rates of the activity generated in the proton beam irradiated volume were 1.58, 1.39, 0.53, 1.08, and 1.85 kcps, respectively. The color line and wash normalized to the iso-center show the dose distribution and activity distribution, respectively. By comparing and verifying between the calculated dose distribution and the measured activity distribution, it can be confirmed visually and roughly that the proton beam has irradiated the tumor. In cases of the liver and the lungs, the length of beam irradiation time is adjusted according to the stability of respiration on the treatment day and the patient. By the effect of organ motion, the number of

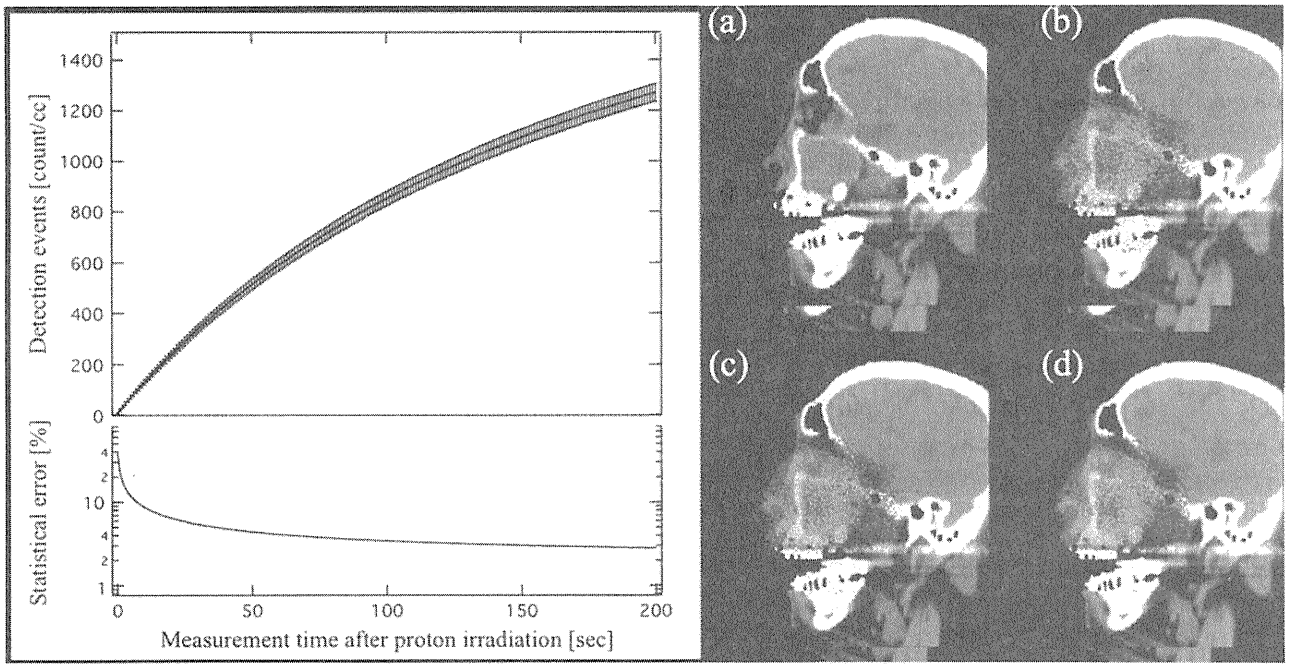

Fig. 3. The number of detection events per volume and PET images obtained during the detection period after proton beam irradiation. The PET images for detection period of (a) 0, (b) 50, (c) 100, and (d) 200 s are shown.

the detection event of the activity measured in the gating window will became about one third of the total detection events, and the statistical error will increase. Therefore, the measurement was performed with no synchronization with organ motion by respiration.

Changes in the activity distribution during the treatment period

In each treatment site, the activity distribution changed probably by reduction of the tumor size and changing of the body shape was conspicuously observed in some cases of the head and neck.

The verification was performed for a case involving tumors of the head and neck. Proton beam irradiation was performed in three fields of view: Port 1: 123 MeV, 90-mm SOBP, 350° gantry angle, 0° bed angle; Port 2: 121 MeV, 90-mm SOBP, 10° gantry angle, 20° bed angle; and Port 3: 117 MeV, 80-mm SOBP, 340° gantry angle, 350° bed angle. The irradiation dose was 2.5 GyE. Figure 5 shows a calculated proton dose distribution, an activity distribution, and a depth profile of a 2.5-GyE dose irradiation after a delivery dose of 2.5 (reference image), 10.0, 17.5, or 32.5 GyE from Port 1, a delivery dose of 5.0 (reference image), 12.5, 20.0, or 35.0 GyE, from Port 2, and a delivery dose of 7.5 (reference image), 15.0, 22.5, or 30.0 GyE from Port 3. Changes of the activity distribution were observed according to changes of the proton beam range and the dose delivered by previous irradiations resulted in a reduction of the tumor (see the arrow and the area surrounded by the dotted line in Fig. 5). The changing values of the activity range for each irradiation field (Port 1, Port 2, and Port 3) are shown in upper left of Fig. 6. The activity range was defined by the depth point of 50% distal falloff in the activity distribution normalized at the iso-center. The changing value of the activity range fully exceeded a 10-mm length. Moreover, to observe the changes in the activity distribution in the depth direction in a similar manner, the ratio of the integration of the detected numbers between 20 mm and 70 mm from the iso-center was expressed as follows:

$$R(D) = \frac{\int_{20}^{70} \left(dA(D)/dZ \right) dz}{\int_{20}^{70} \left(dA(0)/dZ \right) dz}. \quad (1)$$

Here, z is the depth, D is the delivery dose, A(D) is the depth activity distribution, and A(0) is the reference depth activity distribution. The ratio of the delivery dose is shown in the middle left of Fig. 6. The bottom left of Fig. 6 is the proton beam irradiation time per fraction dose at each irradiation. The average of the irradiation time was 30 s, and the difference of the irradiation time at random was within 3 s.

In this case, a new CT image was scanned and a retreatment planning was produced after the delivery of 35 GyE of the prescribed dose of 65 GyE. The volume of the tumor was decreased from 184 mL to 125 mL (the arrow in right of Fig. 6 shows the visible tumor reduction), and the maximum beam range was shortened by 20-mm water equivalent length. In the other 2 cases of 18 clinical cases of the head and neck, the changing activity range of more than 10 mm was observed. Similarly, the new CT image acquisition and the retreatment planning were immediately performed after the observation of the changing activity range. The reduction

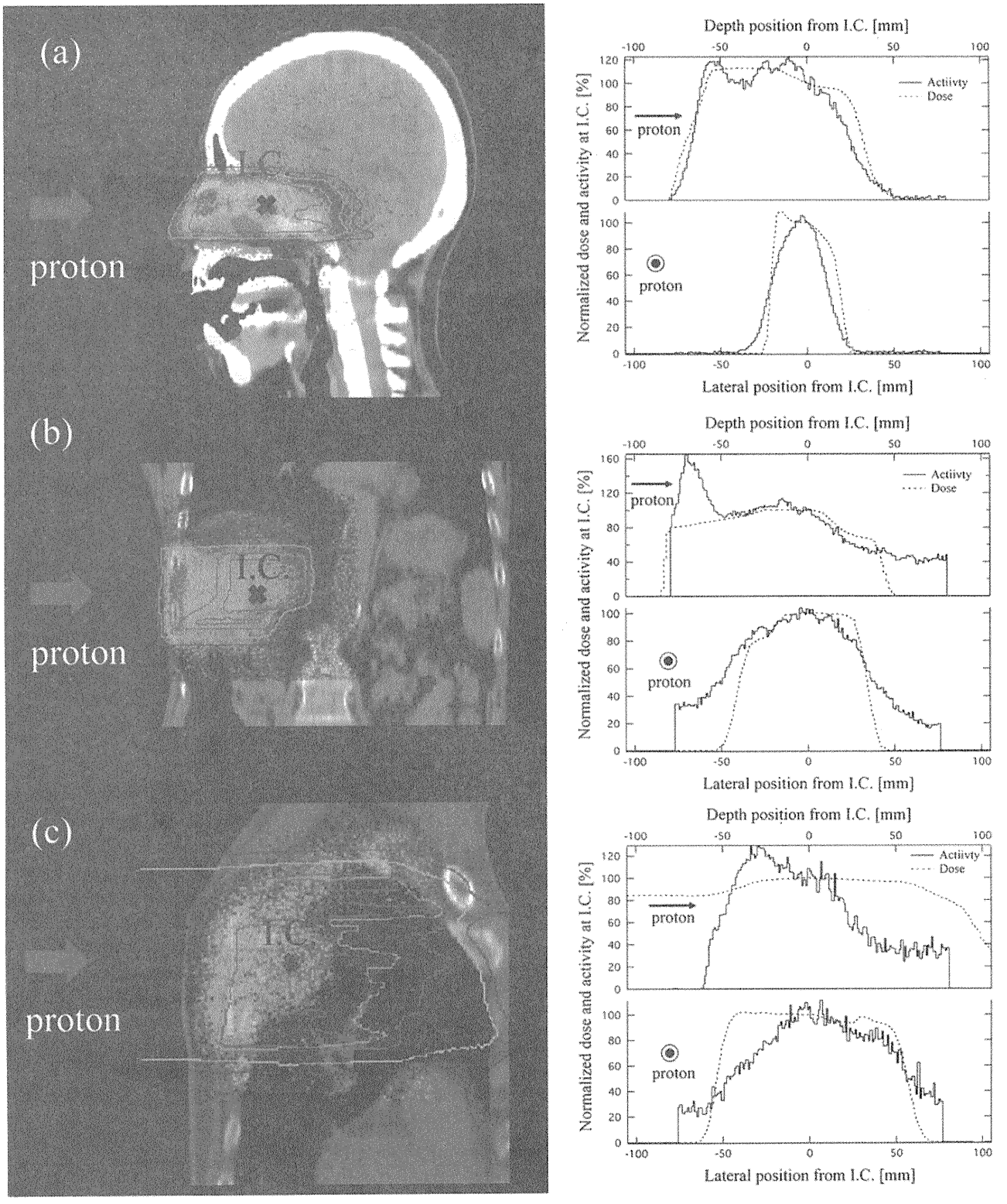

Fig. 4. The calculated dose distribution and the measured activity distribution (left figure), and corresponding lateral and depth profiles (right figure) of the irradiation fields (see Table 1) in each case involving tumors of the head and neck (a), the liver (b), the lungs (c), the prostate (d), and the brain (e), respectively. The iso-dose line of 100% is red, 80% yellowish green, 50% light blue, and 20% purple. The iso-activity wash between 30% and 100% changed from light blue to red.

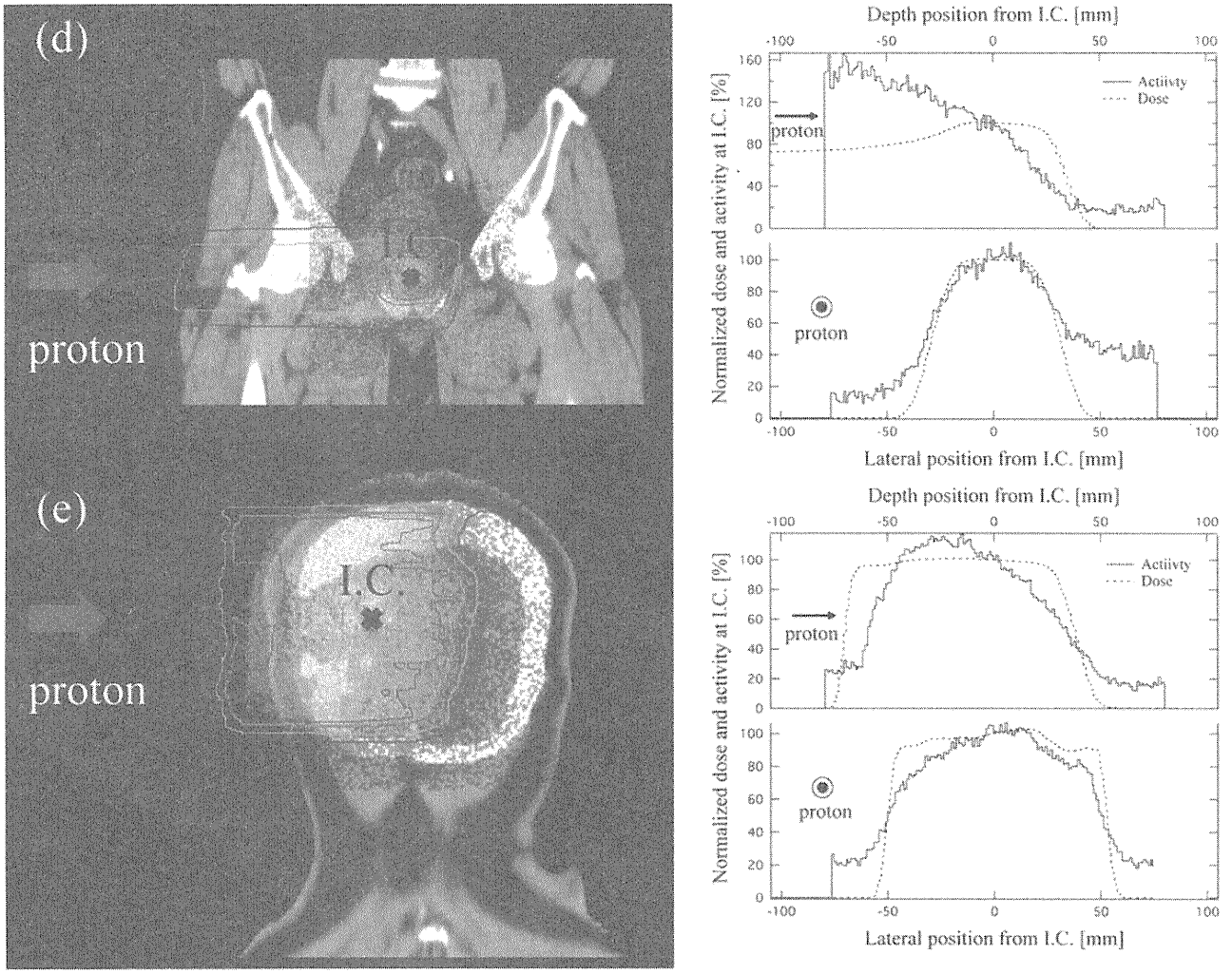

Fig. 4. (*continued*).

of the tumor's volume was more than 100 mL. Also, in carbon therapy, similar observation of the tumor shrinkage has been reported in (7). The BOLPs-RGp indicated that the proton irradiation dose was delivered to the brain stem of organs at risk.

Washout effect of the activity in the treatment period

A histopathologic examination demonstrated that higher activity was observed in regions containing necrotic liver cells than in any other region. The upper panel of Fig. 7 shows the calculated dose distribution and the measured activity distribution on a CT image taken at the first treatment of a 3.8 GyE delivery dose. The bottom left panel of Fig. 7 shows the number of detection counts per 20 s of activity in the regions of interest of areas A and B in the liver. Hence, the region of interest of area A is the necrotic region of the tumor, and area B is the normal tumor region. Therefore, area B-A is equivalent to the area of the tumor minus the necrotic region. The observed decay curves in the region of interest of area A and B-A were fitted well enough using a double exponential equation. The two half-lives of the double exponential fitting were 31 ± 8 s and 146 ± 20 s in the area A, and 21 ± 4 s and 164 ± 11 s in the area B-A, respectively. The half-life was longest in the necrotic region of the tumor. The activity images for the 200 s measurement by the BOLPs-RGp are shown in the left of Fig. 8. The high activity

Table 1. Summary of proton beam irradiation parameters

	Treatment site	Proton energy [MeV]	SOBP [mm]	Gantry angle [deg.]	Bed angle [deg.]	Fractional dose [GyE]	Irradiation time [sec.]
(a)	Head and Neck	123	90	0	0	2.5	39
(b)	Liver	137	70	270	0	3.8	229
(c)	Lungs	145	70	160	0	2.0	38
(d)	Prostate	187	50	270	0	2.0	15
(e)	Brain	122	90	330	90	2.5	40

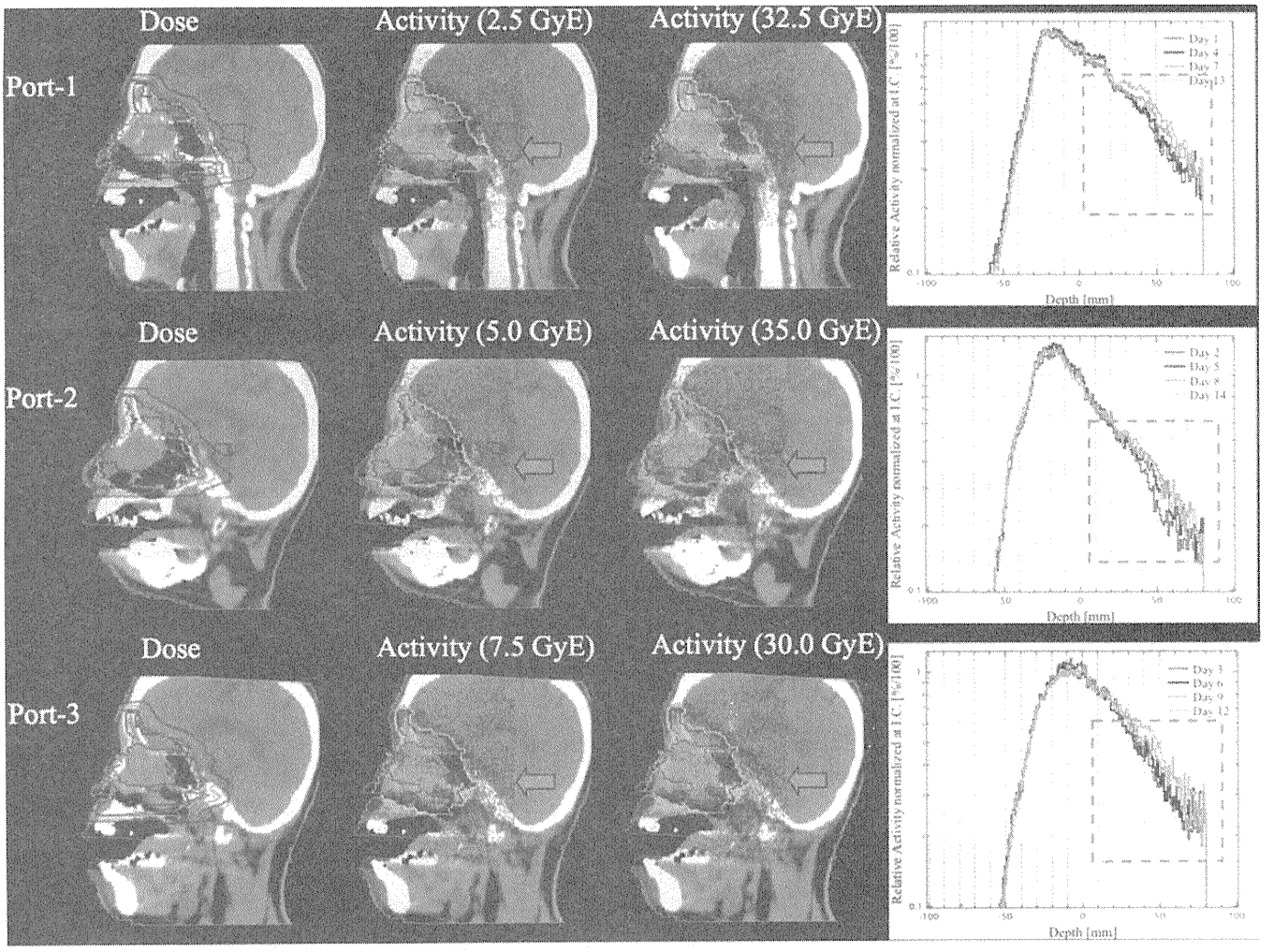

Fig. 5. The calculated proton dose distribution, measured activity distribution of a 2.5-GyE dose irradiation, and the depth profile of the measured activity normalized to the iso-center (0-mm depth) of the reference activity after a delivery dose of 2.5–35.0 GyE.

of the necrotic region decreased to same level as the normal parts of the liver in the last treatment. The ratio F of the detection activity normalized to the activity data from the first treatment for the delivery doses in the area A and the area B-A is expressed as follows:

$$F(D) = \frac{\int_0^{S_A} \left(dN(D)/dS\right) dS / \int_0^{S_A} dS}{\int_{S_A}^{S_B} \left(dN(D)/dS\right) dS / \int_{S_A}^{S_B} dS}. \quad (2)$$

Here, N is the detection number, S_A is the square of area A, and S_B is the square of area B. Ratio of the F values normalized at the value in first treatment calculated by using Eq. 2 and proton beam irradiation time per fraction dose are shown in the right of Fig. 8. The average of the irradiation time at random was 159 ± 77 s. There was no correction in the irradiation time and the decrease of the activity shown in Fig. 8. A decrease in the activity of the necrotic region was observed after the delivery dose was increased without depending on the beam irradiation time per fraction dose.

DISCUSSION

This study focused on the development of the BOLPs-RGp and its clinical use against tumors of the head and neck, liver, lungs, prostate, and brain in the proton therapy. Quick measurement of the activity generated in a patient's body after proton irradiation is feasible by using the BOLPs-RGp. The elements tracked by the activity imaging are ^{11}C (20.39 min), ^{10}C (19.26 s), ^{13}N (9.965 min), ^{15}O (122.2 s), ^{14}O (70.61 s), ^{30}P (2.498 min), and ^{38}K (7.636 min), and according to the results of a simulation by Parodi *et al.*, the "key" positron emitter nuclei are ^{11}C and ^{15}O (14). The measurement of this activity must be immediately performed after proton irradiation as the half-life of ^{15}O is about 2 min. As a result, the information for activity imaging is obtained in a short period. On the other hand, in the case of a beam OFF-LINE PET system used with a commercial based PET or PET/CT apparatus, it is very difficult to measure the activity of ^{15}O for several minutes even at the start of the activity measurement after proton irradiation. The main elements used for activity imaging are ^{15}O for measurements with

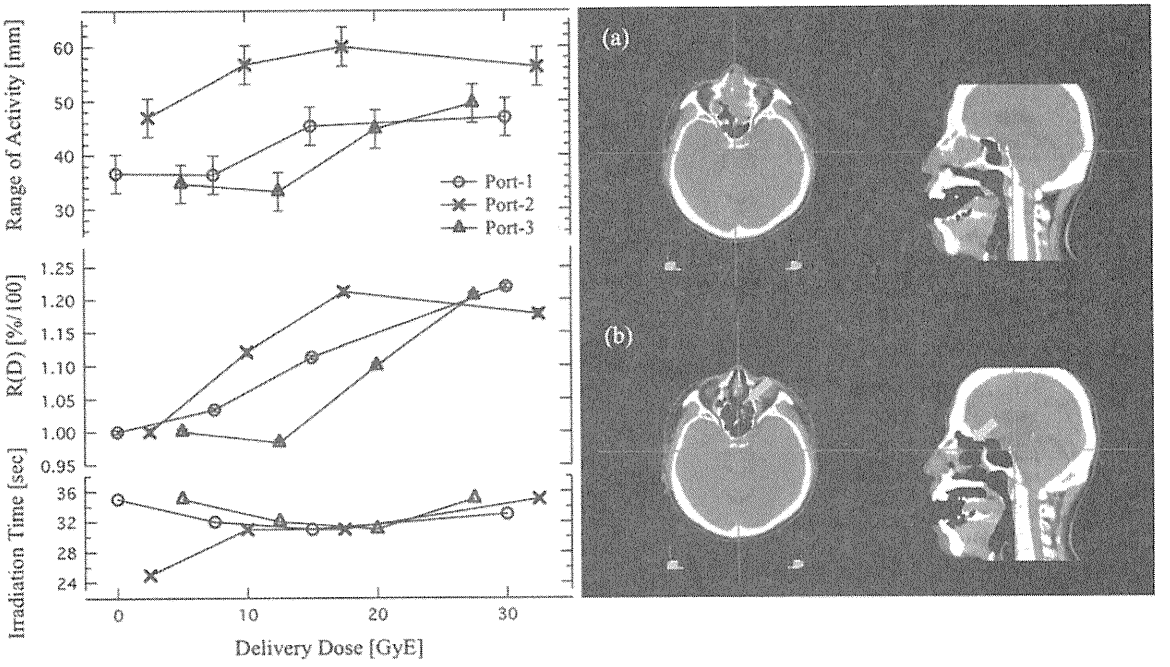

Fig. 6. Changes in the values of the activity range and proton beam irradiation time per fraction dose at each irradiation field of Port-1, Port-2, and Port-3. Axial and sagittal CT images of the head and neck before treatment (a) and after delivery doses of 35 GyE (b).

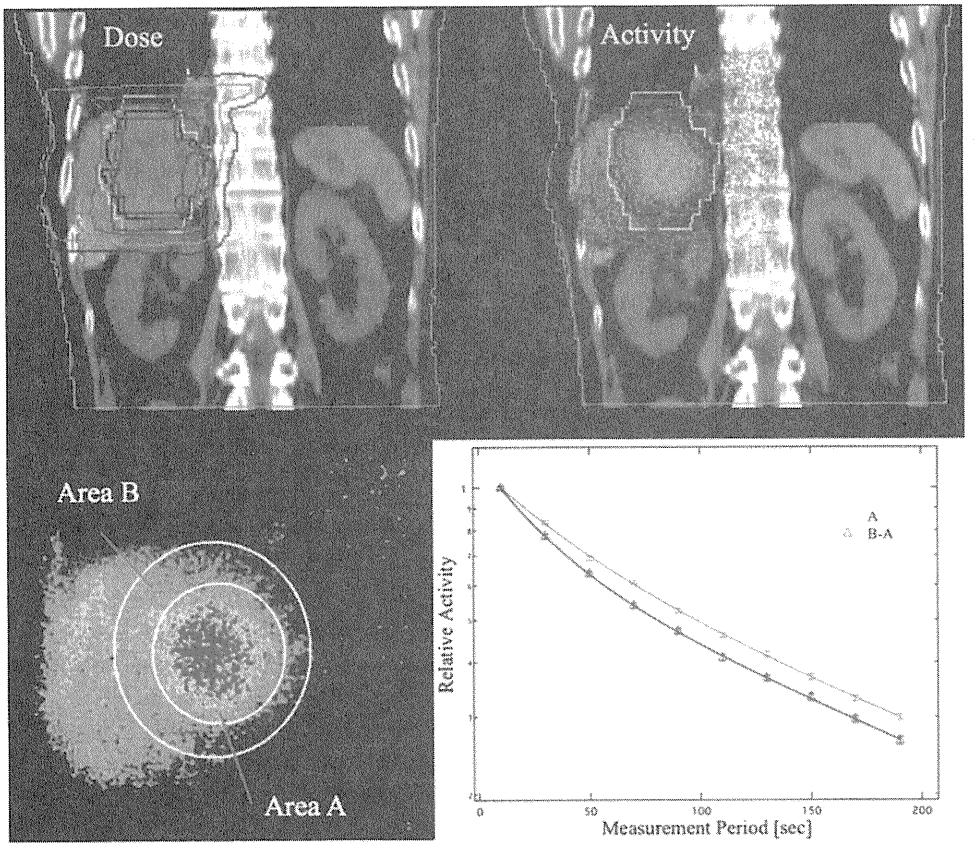

Fig. 7. The calculated dose distribution and the measured activity distribution on a CT image after the first treatment with a 3.8-GyE delivery dose, and the number of detection counts per 20 seconds of the activity in the region of interest (ROI) of areas A and B in the liver.

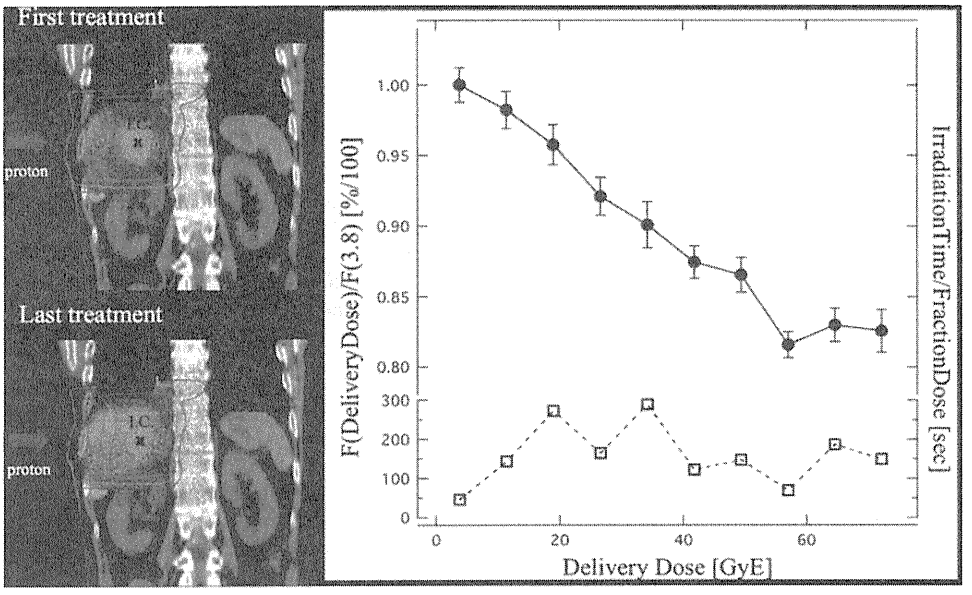

Fig. 8. The activity image and the ratio of the detection number to the measured activity calculated according to Equation (2) in the necrotic region of the liver tumor, and proton beam irradiation time per fractional dose.

the BOLPs-RGp and ^{11}C for measurements with the beam OFF-LINE PET system. As a tumor is equivalent to soft tissue, the measurement of the many ^{15}O nuclei generated in a tumor by proton irradiation is very important for the observation and evaluation of the changing form and the delivery dose response of the tumor. ^{12}C is present and ^{11}C is generated in the adipose tissue. Therefore, high activity is indicated in the region under the skin when using the beam OFF-LINE PET system. Furthermore, the BOLPs-RGp has the advantage of taking measurements with the patient in same position during proton irradiation. However, the CT image for the patient positioning can not be acquired at the same time as the activity measurement when using the BOLPs-RGp. This problem can be solved by the technological introduction of a CBCT.

At present, the length of activity measurement with the BOLPs-RGp after proton beam irradiation is 200 s; but, it may be possible that the measurement time can be shortened to less than 200 s as a result of this research. However, the measurement time must be determined with consideration to the detection efficiency by the delivery dose of each treatment site, the distance between the detector heads, and the activity measurement synchronized with the organ motion caused by respiration in the case of the liver and lungs.

The BOLPs-RGp has been used in the daily proton treatment of 48 patients. The monitoring of the accuracy of the proton beam irradiation was performed by comparing and verifying the daily activity images with reference activity images obtained at the start of the proton treatment. Specially, optimized proton treatment was performed by quickly replanning treatment in three clinical cases involving head-and-neck tumors, because different activity distribution were observed in the two images during the treatment period. The decrease of the activity in the region of necrotic cells in the liver tumor found during the histopathological examination was linked to an increase in the delivery dose. It is suggested that the increase in the washout effect in the necrotic region is caused by a decrease in the number of necrotic cells in the liver because of increased blood flow caused by the higher proton delivery dose. This effect may indicate a need to adapt the treatment to the dose response of the tumors in individual patients as well as the observation of the functional metabolism of organs.

The quality of the activity image is reduced by the large organ motion of the liver and the lungs. In cases of the prostate, the verification of changes in the activity distribution against the condition of the bladder and the position of the head of the femur will be reported in future. Moreover, a study concerning the experimental determination of cross sections of the target nuclear fragment reaction has been completed, and a simulation system that includes our cross-section data for calculating activity distribution in a patient's body with a high accuracy has been constructed using a cluster computer system. Many results of the research of the simulation have been already reported by the study group of Parodi *et al.* (12, 14). Finally, the ideal DGPT will be achieved through these developments and the research.

CONCLUSIONS

A BOLPs-RGp was constructed in our proton treatment room. The BOLPs-RGp has been used in many clinical cases. Report of the clinical use with beam ON-LINE PET or in-beam PET in the proton therapy has been never done before. The daily activity images obtained indicated the proton irradiation volume of the treatment administered to patients. Information about the positron-emitting nuclei provided by the BOLPs-RGp will be important for improving proton treatment accuracy in the future. DGPT (10) will thereby be achieved via daily proton treatment using the BOLPs-RGp.

REFERENCES

1. Oelfke U, Lam G, Atkins M. Proton dose monitoring with PET: Quantitative studies in Lucite. *Phys Med Biol* 1996;41: 177–196.
2. Litzenberg DW, Roberts DA, Lee MY, *et al.* On-line monitoring of radiotherapy beams: Experimental results with proton beams. *Med Phys* 1999;26:992–1006.
3. Parodi K, Enghardt W. Potential application of PET in quality assurance of proton therapy. *Phys Med Biol* 2000;45:N151–N156.
4. Nishio T, Ogino T, Shimbo M, *et al.* Distributions of b^+ decayed nucleus produced from the target fragment reaction in $(CH_2)n$ and patient liver targets by using a proton beam for therapy. *Abstr XXXIV PTCOG Mtg Boston* 2001;15–16.
5. Parodi K, Enghardt W, Haberer T. In-beam PET measurements of β^+ radioactivity induced by proton beams. *Phys Med Biol* 2002;47:21–36.
6. Hishikawa Y, Kagawa K, Murakami M, *et al.* Usefulness of positron-emission tomographic images after proton therapy. *Int J Radiat Oncol Biol Phys* 2002;53:1388–1391.
7. Enghardt W, Parodi K, Crespo P, *et al.* Dose quantification from in-beam positron emission tomography. *Radiother Oncol Suppl 2* 2004;73:S96–S98.
8. Nishio T, Sato T, Kitamura H, *et al.* Distributions of β^+ decayed nuclei generated in the CH_2 and H_2O targets by the target nuclear fragment reaction using therapeutic MONO and SOBP proton beam. *Med Phys* 2005;32:1070–1082.
9. Parodi K, Ponisch F, Enghardt W. Experimental study on the feasibility of in-beam PET for accurate monitoring of proton therapy. *IEEE Trans Nucl Sci* 2005;52:778–786.
10. Nishio T, Ogino T, Nomura K, *et al.* Dose-volume delivery guided proton therapy using beam ON-LINE PET system. *Med Phys* 2006;33:4190–4197.
11. Parodi K, Paganetti H, Cascio E, *et al.* PET/CT imaging for treatment verification after proton therapy: A study with plastic phantoms and metallic implants. *Med Phys* 2007;34: 419–435.
12. Parodi K, Paganetti H, Shih HA, *et al.* Patient study of in vivo verification of beam delivery and range, using positron emission tomography and computed tomography imaging after proton therapy. *Int J Radiat Oncol Biol Phys* 2007;68:920–934.
13. Nishio T, Miyatake A, Inoue K, *et al.* Experimental verification of proton beam monitoring in a human body by use of activity image of positron-emitting nuclei generated by nuclear fragmentation reaction. *Radiol Phys Technol* 2008;1: 44–54.
14. Parodi K, Ferrari A, Sommerer F, *et al.* Clinical CT-based calculations of dose and positron emitter distributions in proton therapy using the FLUKA Monte Carlo code. *Phys Med Biol* 2007;52:3369–3387.
15. Pawelke J, Enghardt W, Haberer T, *et al.* In-beam PET imaging for the control of heavy-ion tumour therapy. *IEEE Trans Nucl Sci* 1997;44:1492–1498.
16. Parodi K, Crespo P, Eickhoff H, *et al.* Random coincidences during in-beam PET measurements at microbunched therapeutic ion beams. *Nucl Instrum Meth A* 2005;545:446–458.
17. Uchida H, Okamoto T, Ohmura T, *et al.* A compact planar positron imaging system. *Nucl Instr Meth* 2004;A516:564–574.

Neurol Med Chir (Tokyo) 49, 340 ~ 350, 2009

Clinical Indications for High-Field 1.5 T Intraoperative Magnetic Resonance Imaging and Neuro-navigation for Neurosurgical Procedures

—Review of Initial 100 Cases—

Satoshi MAESAWA, Masazumi FUJII*, Norimoto NAKAHARA, Tadashi WATANABE, Kiyoshi SAITO*, Yasukazu KAJITA*, Tetsuya NAGATANI*, Toshihiko WAKABAYASHI*, and Jun YOSHIDA*

Department of Neurosurgery, Nagoya Central Hospital, Nagoya, Aichi;
**Department of Neurosurgery, Nagoya University Graduate School of Medicine, Nagoya, Aichi*

Abstract

Initial experiences are reviewed in an integrated operation theater equipped with an intraoperative high-field (1.5 T) magnetic resonance (MR) imager and neuro-navigation (BrainSUITE®), to evaluate the indications and limitations. One hundred consecutive cases were treated, consisting of 38 gliomas, 49 other tumors, 11 cerebrovascular diseases, and 2 functional diseases. The feasibility and usefulness of the integrated theater were evaluated for individual diseases, focusing on whether intraoperative images (including diffusion tensor imaging) affected the surgical strategy. The extent of resection and outcomes in each histological category of brain tumors were examined. Intraoperative high-field MR imaging frequently affected or modified the surgical strategy in the glioma group (27/38 cases, 71.1%), but less in the other tumor group (13/49 cases, 26.5%). The surgical strategy was not modified in cerebrovascular or functional diseases, but the success of procedures and the absence of complications could be confirmed. In glioma surgery, subtotal or greater resection was achieved in 22 of the 31 patients (71%) excluding biopsies, and intraoperative images revealed tumor remnants resulting in the extension of resection in 21 of the 22 patients (95.4%), the highest rate of extension among all types of pathologies. The integrated neuro-navigation improved workflow. The best indication for intraoperative high-field MR imaging and integrated neuro-navigation is brain tumors, especially gliomas, and is supplementary in assuring quality in surgery for cerebrovascular or functional diseases. Immediate quality assurance is provided in several types of neurosurgical procedures.

Key words: intraoperative magnetic resonance imaging, navigation, glioma

Introduction

Intraoperative magnetic resonance (MR) imaging has gradually become widespread since Brigham and Women's Hospital in Boston introduced a 0.5 Tesla (T) open MR imager to the operating theater in 1994.[2,5,24,40,41] Our institution installed a fully integrated neurosurgical system including neuro-navigation and an intraoperative 1.5 T high-field MR imager (BrainSUITE®; BrainLAB AG, Heimstetten, Germany), the first such unit in Asia, in 2006. Compared to intraoperative low- or medium-field MR imaging, this system provides high quality images with short scan times, and various sequences are available intraoperatively including MR spectroscopy, diffusion tensor imaging, diffusion-weighted imaging, and MR angiography.[27,28,31,32] Using an image-fusion technique, the integrated navigation system can combine MR imaging data with functional and/or metabolic information obtained by other modalities such as positron emission tomography (PET) and magnetoencephalography.[9,27] Overall, the fully integrated architecture facilitates straightforward workflow including patient transport, image

Received May 23, 2008; Accepted February 13, 2009
Author's present address: S. Maesawa, M.D., Department of Neurosurgery, Nagoya University Graduate School of Medicine, Nagoya, Aichi, Japan.

scanning, image fusion, surgical planning, registration for navigation, and updating of navigation images. The progenitor of our system was first described by the Erlangen University group, and that system has been improved stepwise over a number of years.[32] Our system is a fully integrated architecture incorporating such improvements, so is almost functionally equal to the current system in Erlangen. In the first year following installation, we operated mainly on brain tumors, but also other diseases including cerebrovascular and functional diseases. The effectiveness and feasibility of intraoperative MR imaging for these diseases is still controversial.[6,42]

The present study describes the layout and features of our intraoperative MR imaging system, and analyzes our initial experiences of 100 consecutive procedures performed in the first year, and discuss the indications and limitations of this system.

Materials and Methods

I. Features of the operation theater

Figure 1 shows the appearance of our 10.5 × 6.6 m operating room, BrainSUITE®. The walls, floor, and ceiling contain radiofrequency shielding based on aluminum and copper mesh. The high-field-strength (1.5 T) MR imager (Magnetom Symphony; Siemens Healthcare, Erlangen, Germany) consists of a superconductive magnet with a length of 160 cm and an inner bore diameter of 60 cm, and a gradient system with a maximum field strength of 30 mT/m and an effective slew rate of 125 T/m/sec. The performance is equivalent to systems used for diagnostic imaging. An elliptical line (8-m major and 5-m minor axis) is drawn around the scanner to mark the 5-gauss field limit for safety. The operating table is positioned parallel to the scanner during surgery so that the patient's head lies outside the 5-gauss line. Therefore, standard surgical instruments can be used regardless of magnetic properties (ferromagnetic or non-ferromagnetic). The connection between the table and head-holder is a ball-and-socket joint that allows the head-holder orientation to be freely adjusted. When imaging is necessary, the table is rotated manually by 180 degrees about a vertical axis to align it with the scanner bore.

The head-holder has a bivalve shape, consisting of two parts, and contains an 8-channel receiver array. The upper part of the head-holder is sterilized with plasma and placed above the operating field for MR imaging, but is removed during surgery. Rapid automatic image registration is realized with a reference array attached to the upper part of the head-holder. The array contains 14 MR imaging-visible fiducial markers as well as 4 infrared reflector spheres that are continuously tracked by a ceiling-mounted infrared camera. Navigation is accomplished with an error of less than 0.6 mm.

The anesthesia equipment is MR imaging-compatible (Estiva 5; Datex-Ohmeda, Inc., Madison, Wisc., U.S.A.). Inhalation and exhalation ducts are approximately 6 m in length to allow the table to rotate and move into the scanner. The neuro-microscope (NC4 multivision scope; Zeiss, Oberkochen, Germany) is ceiling-mounted outside the 5-gauss line. Navigation-related information is sent to the neuro-microscope so that the configuration of objects (e.g. tumor and pyramidal tract) can be superimposed over the surgical field in the microscope view. Surgical equipment in contact with the patient's body (e.g., scalp clamps, aneurysm clips) must be MR imaging-compatible to prevent burns and image degradation.

II. Patient population

One hundred consecutive patients, 51 males and 49 females aged 13 to 80 years (mean 50.7 years), were treated in the BrainSUITE® at Nagoya Central Hospital between August 2006 and August 2007. Surgeries that were thought to have the potential to benefit from intraoperative MR imaging and navigation were scheduled. Emergency surgeries were not performed. Patients were treated for brain tumors (n = 87, 87%), vascular diseases (n = 11, 11%), and functional diseases (n = 2, 2%). Histological examinations revealed gliomas (n = 38; World Health Organization grade 2 n = 7, grade 3 n = 10, glioblastoma multiforme n = 21), meningioma (n = 14), pituitary adenoma (n = 9), metastatic tumor (n = 9), schwannoma (n = 6), craniopharyngioma (n = 3), germinoma (n = 2), malignant lymphoma (n = 2), epidermoid (n = 1), cavernoma (n = 1), tuberculoid granuloma (n = 1), and arachnoid cyst (n = 1). Craniotomy and tumor removal were performed in 70 patients (70/87), and navigation-based stereotactic biopsy was performed in 17 patients (17/87). Surgery for vascular diseases consisted of clipping for cerebral aneurysms (n = 7; unruptured 6, ruptured 1), superficial temporal artery-middle cerebral artery (STA-MCA) bypass for internal carotid artery occlusion (n = 3), and removal of an arteriovenous malformation (n = 1). Surgery for functional diseases included subthalamic nucleus-deep brain stimulation (STN-DBS) for advanced Parkinson's disease (n = 1), and microvascular decompression (MVD) for trigeminal neuralgia (n = 1). The local ethical committee approved the clinical utilization of intraoperative high-field MR imaging as well as the navigation system, and signed informed consent was

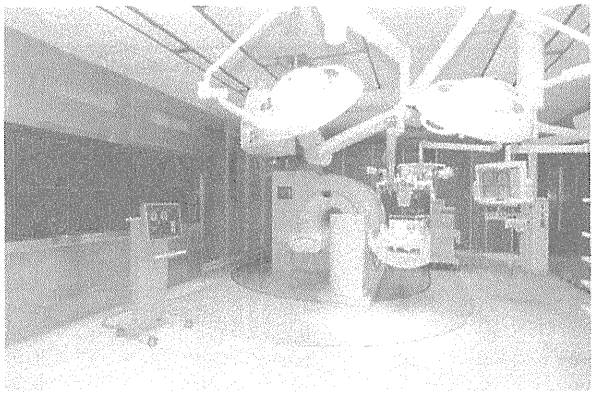

Fig. 1 Photograph showing the integrated intraoperative magnetic resonance imaging and neuro-navigation system (BrainSUITE®): The 50-gauss (*red*) and 5-gauss (*yellow*) lines are marked on the floor. The imager, operating table, and operating microscope are all integrated with the navigation system.

provided by all patients prior to surgery.

III. Brain tumor surgery

Surgical planning was based on multiple sequences of MR images taken 1 or 2 days before surgery. Target lesions and important anatomical structures were coded as colored objects (Fig. 2A). Image fusion was used to integrate and display metabolically interesting areas of gliomas suggested by [^{18}F]fluorodeoxyglucose-PET, [^{11}C]L-methionine-PET, or MR spectroscopy. Diffusion tensor imaging was performed to visualize the major white matter tracts such as the pyramidal tract or optic radiation. Preoperative functional MR imaging was used to identify the primary motor cortex or language centers. On the day of surgery, the first MR imaging was performed after positioning, but before the operation started, to provide a reference for navigation (reference MR image). This process was necessary to ensure a low registration error. The preoperatively coded objects described above were then incorporated through automatic image registration and fusion, a process requiring less than 20 seconds. During craniotomy and microsurgery, standard surgical instruments were utilized. If the tumor was located in or around the pyramidal tract, electrophysiological monitoring such as somatosensory-evoked potential and/or motor-evoked potential (MEP) monitoring was used (Bravo; Nicolet Biomedical, Madison, Wisc., U.S.A.) in combination with diffusion tensor imaging tractography.

Intraoperative MR imaging was performed when the surgeon considered that the goal of surgery had

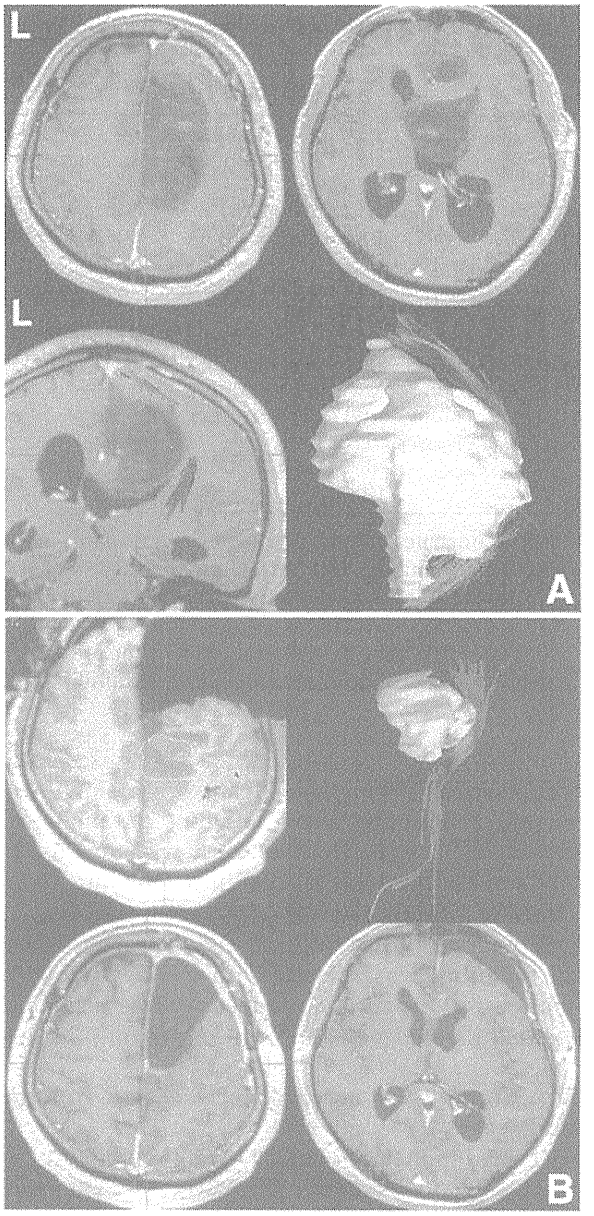

Fig. 2 A 35-year-old male with an anaplastic astrocytoma in the right frontal lobe extending to the third ventricle. A: Preoperative magnetic resonance (MR) images (*upper row*) and surgical planning images (*lower row*) showing the pyramidal tract (*rainbow*) and the tumor (*yellow*). The pyramidal tract was shifted posterior and laterally by the tumor. B: Intraoperative MR images (*upper row*) revealing a tumor remnant (*orange line*) anterior to the pyramidal tract, resulting in resumption of resection, and total removal of the tumor (*lower row*). The patient developed hemiplegia postoperatively, which completely resolved after 1 week (supplementary motor area syndrome).

Table 1 Sequences and parameters used in BrainSUITE®

	Sequences	TR (msec)	TE (msec)	TI (msec)	FA (°)	FOV (mm)	Thickness (mm)	No. of slices	Parallel imaging	Scan time (min.sec)
Tumors (gliomas)	3D T1WI (3D FLASH)	11	5.2	0	15	282	1.1	160	–	5.06
	3D T1WI (3D MPRAGE)	2160	4.38	1100	15	282	1.1	160	+	3.55
	3D T2WI (3D TSE)	3200	580	0	variable	282	1.1	160	+	4.43
	3D FLAIR (3D TSE)	6000	402	0	variable	282	2.2	64	+	4.50
	DTI (SE-EPI)	7500	99	0	90	320	2.5	50	+	5.39
	CSI	1600	135	0	90	120×120	20.0	1	–	7.41
	fMR imaging (FID-EPI)	3500	50	0	90	192	3.0	35	–	4.16
Pituitary tumors	2D T2WI (2D TSE)	3630	105	0	90	190	1.6	14	+	5.50
	3D T1WI (3D FLASH VIBE)	10	3.65	0	12	190	0.7	128	+	6.32
Vascular diseases	DWI (SE-DWI)	3500	107	0	90	260	5.0	19	+	1.19
	MR angiography (3D TOF)	39	7.1	0	25	240	0.9	40	+	6.05
	PWI (FID-EPI)	230	1000	0	90	40	5.0	10	+	1.28
Functional diseases	2D STIR	8900	92	180	180	230	1.5	25	+	7.18
	3D T1WI (3D FLASH)	11	5.2	0	15	282	1.1	160	–	5.06
	CISS	10.18	5.09	0	70	200	0.8	60		5.46

CISS: constructive interference in steady state, CSI: chemical shift imaging, 3(2)D: three(two)-dimensional, DTI: diffusion tensor image, DWI: diffusion-weighted image, EPI: echo planar image, FA: flip angle, FID: free induction decay, FLASH: fast low-angle shot, fMR: functional magnetic resonance, FOV: field of view, MPRAGE: magnetization prepared rapid gradient echo, PWI: perfusion-weighted image, SE: spin echo, STIR: short time to inversion recovery, TE: echo time, TI: time to inversion, TOF: time of flight, TR: repetition time, TSE: turbo spin echo, T1(2)WI: $T_{1(2)}$-weighted image, VIBE: volume interpolated breath-hold examination.

been met, or after a significant brain shift had occurred. Frequently used imaging parameters are shown in Table 1. Contrast enhancement used 0.2 ml/kg of gadolinium. Diffusion tensor imaging was obtained intraoperatively as well.[29] If intraoperative MR imaging indicated incomplete resection, surgical planning was revised with the newly obtained images, and the surgical procedure was resumed under the updated navigation information (Fig. 2B).

IV. Surgery for cerebrovascular and functional diseases

Three-dimensional (3-D) T_1-weighted MR imaging (fast low-angle shot [FLASH], magnetization-prepared rapid gradient-echo), MR angiography, and diffusion-weighted MR imaging were performed before and after clipping surgery. Navigation was employed in some cases, including one complex aneurysm of the anterior communicating artery. Constructive interference in the steady state (CISS) MR imaging was added before and after MVD in a patient with trigeminal neuralgia. Frame-based stereotaxy was performed with a Leksel stereotactic frame (Elekta, Stockholm, Sweden) to treat Parkinson's disease with STN-DBS. 3-D FLASH MR imaging and short time inversion recovery MR imaging were performed after loading the frame for the initial targeting. Microelectrode recording was performed (Lead-Point®; Medtronics, Minneapolis, Minn., U.S.A.) for electrophysiological confirmation. To assure positional accuracy after electrode implantation, 3-D FLASH imaging was acquired with the specific absorption rate limited to 0.1 W/kg or less following the safety guidelines recommended by Medtronics.[37]

V. Data analysis

Each procedure was evaluated with respect to the usefulness of intraoperative images and navigation, technical problems, and patient outcomes. Any effect of intraoperative MR imaging on the surgical strategy was also documented, such as extension of the tumor resection, or correction of the catheter, electrode, or biopsy needle position. The extent of the brain tumor resection was calculated based on manual segmentation of the tumor outline in the planning software. Glioma volume was defined as the volume of increased intensity on T_1-weighted images with contrast medium. Tumor volume for non-enhanced tumors was defined as the area of increased intensity on T_2-weighted images. Subtotal or greater resection was defined as more than 95% of the tumor volume absent postoperatively. We did not use the term total resection for gliomas because of their characteristic infiltrating progression. The postoperative neurological condition of all patients was documented.

Table 2 Modification of surgical strategy by intraoperative magnetic resonance images in BrainSUITE®

	Subgroups	No. of cases		Percentage
		Total	With modification	
Glioma	overall	38	27	71.1
	subtotal resection	22	21	95.4
	partial resection	9	6	66.6
	biopsy	7	0	0
Pituitary tumor	overall	9	4	44.4
	total resection	7	3	42.8
	partial resection	2	1	50
Meningioma	overall	14	2	14.2
	total resection	13	1	7.6
	partial resection	1	1	100
Schwannoma	overall	6	1	16.7
	total resection	5	0	0
	partial resection	1	1	100
Metastatic tumor	overall	9	3	33.3
	total resection	5	1	20
	biopsy/cyst aspiration	4	2	50
Others	overall	11	3	27
	total resection	5	2	40
	biopsy/cyst aspiration	6	1	16.7
Vascular diseases		11	0	0
Functional diseases		2	0	0
Total		100	40	40

Results

Intraoperative MR imaging, including reference MR imaging, was performed 242 times during the 100 procedures. No incident was caused by the ferromagnetic instruments. The period of interruption for each intraoperative MR imaging session was approximately 20 minutes, depending on the imaging sequences. Intraoperative MR imaging affected the surgical strategy in 40 of the 100 cases, most frequently in the glioma group (27/38), and less so in the other tumor group (13/49). These results are summarized in Table 2. The surgical strategy was not modified after intraoperative MR imaging for cerebrovascular or functional diseases, but intraoperative MR imaging confirmed the success of each procedure while the patient was still on the operating table.

I. Glioma surgery

Gliomas (n = 38) were located as follows: frontal lobe, n = 18; temporal lobe, n = 2; parietal lobe, n = 3; occipital lobe, n = 1; frontoparietal lobe, n = 3; frontotemporal lobe, n = 2; temporo-occipital lobe, n = 4; insula, n = 2; thalamus, n = 1; and cerebellum, n = 2. Craniotomy and tumor resection were performed in 31 cases, and navigation-guided biopsy in 7 cases. Intraoperative MR imaging was taken 2 to 5 times (mean 2.8). Intraoperative MR imaging modified the surgical strategy in 27 of the 38 patients. Subtotal or greater resection was achieved in 22 of the 31 cases. Intraoperative imaging revealed tumor remnants in 21 of these 22 cases, resulting in the resumption of surgery. A representative case is shown in Fig. 2. Some tumor was intentionally left to prevent neurological deterioration in 10 cases. Intraoperative imaging contributed to the identification of the optimal location and volume of the intentional remnant in 6 of these 10 cases. Diffusion tensor imaging-based tractography was performed combined with MEP monitoring (employing transcortical and direct white matter stimulation) in 19 cases, and without MEP monitoring in 25 cases. Postoperatively, 5 patients showed transient deterioration of motor functions, but improved to the baseline within 1 day to 2 weeks. One patient experienced wound infarction which required debridement later. One patient with glioblastoma arising from the medial thalamus developed deep vein infarction postoperatively, and suffered from prolonged disturbance of consciousness. This was the most severe complication in the series.

II. Other tumor surgeries

Intraoperative MR imaging was performed 2 to 3

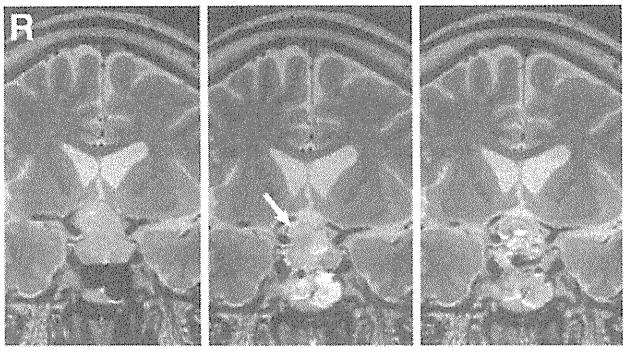

Fig. 3 A 51-year-old male with a non-functional pituitary adenoma treated through an endoscopic transnasal approach. Preoperative (*left*) and intraoperative magnetic resonance (MR) images (*middle*) revealing a tumor remnant behind the fold of the arachnoid membrane (*arrow*), which was not visible through the endoscope, and final intraoperative MR image (*right*) confirming complete resection.

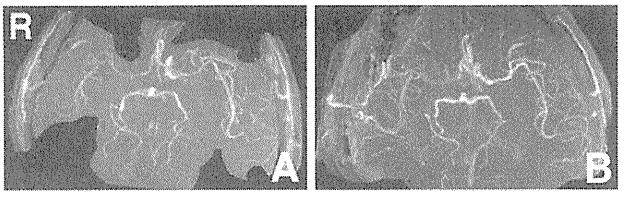

Fig. 4 A 49-year-old male with right internal carotid artery occlusion treated by right double superficial temporal artery-middle cerebral artery (MCA) anastomoses. Intraoperative magnetic resonance (MR) imaging was taken before and after anastomoses, including MR angiograms (A, B). Immediately following anastomoses, MR angiograms showed good patency of the bypass and improved delineation of vascularity in the MCA area.

times (mean 2.2). Overall, gross total resection was achieved in 35 of the 39 cases, excluding 10 biopsy cases (Table 2). Intraoperative imaging revealed tumor remnants in 7 patients. Simpson grade 2 or better resection was achieved in all cases of meningioma (n = 14) except for one. Image fusion with the bone window 3-D computed tomography was useful if the tumor was located at the skull base. Pituitary adenomas (n = 9) were treated through a transcranial approach in 4 cases and endoscopic transnasal approach in 5 cases. Total resection was achieved in 7 cases. The endoscope and instruments were used without complications outside the 5-gauss line. Besides 3-D T_1-weighted images, thin slice sagittal and coronal T_2-weighted images were useful to identify tumor remnants (Fig. 3). For schwannoma cases (n = 6), total resection was performed in 5 cases. For metastatic tumors (n = 9), total resection was performed in 5 cases, and biopsy or aspiration of the cyst was performed in the remaining cases. The surgical strategy was frequently modified following intraoperative MR imaging for pituitary adenomas (44.4%) as well as for metastatic tumors (33.3%) as summarized in Table 2.

III. Surgery for cerebrovascular and functional diseases

MR angiography showed good patency of the anastomosis site in all cases of STA-MCA anastomosis (n = 3) (Fig. 4). MR angiography had difficulties in evaluating the vasculature around the clipping site due to artifacts. However, diffusion-weighted imaging was useful to rule out acute ischemic complications.

Microelectrode recording was successfully performed using the ordinary device in the STN-DBS procedure. The magnetic field did not interfere with the recording, and the signal/noise ratio was better than that recorded in a standard operating room. The 3-D T_1-weighted imaging (FLASH) demonstrated correct placement of the electrode. CISS images clearly demonstrated that the decompression was successful after MVD for trigeminal neuralgia.

Discussion

High-field intraoperative MR imaging has several advantages over low-field MR imaging. The quality of intraoperative images obtained at a high field is almost equal to that of preoperative images, and this leads to more reliable information derived from the visualization of anatomical structures and residual tumor. The higher intrinsic signal/noise ratio with a high field allows us to acquire a higher spatial resolution in a given scan time. Various sequences are available. Diffusion tensor imaging, which is feasible with high-field but is difficult with low-field MR imaging, can visualize the course of subcortical tracts. Obvious disadvantages of high-field MR imaging are the high initial cost, the large space required due to the relatively wide magnetic fringe field, and the necessity for extra safety precautions in the vicinity of the super-conducting magnet.

The best use for the integrated navigation and intraoperative high-field MR imaging system seems to be glioma surgery. In our series of gliomas, the rate

of greater than subtotal resection was 71%, which is almost equal to or better than the rates reported previously.[15,16,25,38] The findings of intraoperative imaging modified the surgical strategy in 71.1% of patients with gliomas, the highest among our cases of brain tumors, indicating that glioma surgery was the best indication.

This system provides three advantages for glioma surgery. Firstly, updating navigation with intraoperative images compensated for the "brain shift" caused by withdrawal of cerebrospinal fluid and/or mass reduction of the tumor. Secondly, high-field MR imaging could provide diffusion tensor imaging-based tractography intraoperatively. Less than 10 minutes was required for both measurement of diffusion tensor imaging and computation of tractography. Artifacts were seen at the surface of the brain, but not at subcortical locations, so this technique was especially useful for visualizing the subcortical tracts. The importance of tractography for the preservation of motor function in gliomas is well known.[12,34] However, brain shift must also be considered. The maximum shift in white matter is reported to range from −8 to −15 mm intraoperatively,[30,31] consistent with our experience. Since our system allowed tractography to be updated intraoperatively, safety was maintained even after the brain shift had occurred. Furthermore, the combination of tractography and MEP monitoring with direct white matter stimulation improved monitoring accuracy.[1,13,14,21] We found that tractography based on intraoperative diffusion tensor imaging localized the pyramidal tract (as identified by direct white matter stimulation) more accurately than preoperative diffusion tensor imaging, and this finding will be reported in detail elsewhere. The occurrence of postoperative transient paresis was probably high in our series, but might reflect our surgical approach nearly to the tumor boundary. Thirdly, our system could fuse navigation with other modalities such as PET and MR spectroscopy, thus improving the accuracy of the histological diagnoses. Gliomas exhibit tumor-heterogeneity to varying degrees, so metabolic information should be used to guide biopsies.[20,26,27] Although image fusion is available for standard navigation, our system is advantageous because we can confirm the position of the collected specimen immediately after the procedure by intraoperative MR imaging. In general, extending glioma resection as far as possible prolongs patient survival.[15,16] Long-term follow up is necessary to reveal whether surgical management with this integrated navigation and intraoperative MR imaging system leads to an improved prognosis.

Considering the indication for other tumors, we believe that pituitary adenomas are also a good indication. The percentage of surgeries modified by intraoperative MR imaging (44.4%) was the second highest following gliomas. Even with endoscopic assistance, tumor remnants are not readily discriminated from the normal pituitary gland. The blind side behind the fold of the arachnoid and the descending sella diaphragm is another problem. Intraoperative MR imaging could identify tumor remnants which indicated further resection, as similarly described previously.[7,33] Metastatic tumors have relatively identifiable boundaries, but some demonstrate infiltrative characteristics so that intraoperative MR imaging was useful to achieve complete resection. Meningiomas, schwannomas, and other extra-axial tumors have a clear margin, so the need for intraoperative imaging was reduced. However, both intraoperative images and navigation were found to be helpful if some of the tumor was intentionally left to preserve functional structures.

Vascular reconstructive surgery is a possible indication. Our results showed good patency of the anastomotic vessels by MR angiography, which confirmed surgical success. We experimentally performed perfusion-weighted imaging before and after anastomosis, using the analysis method previously recommended.[35] Various imaging findings have been reported after vascular reconstructive surgery,[4,8,43,45] but our imaging study in the superacute postoperative period might contribute to the prediction of hyperperfusion syndrome, or to intraoperative control for anesthesia. Further study is necessary to clarify its importance. Intraoperative MR images were less useful in clipping surgery. An important issue was clip-induced artifacts which complicated the evaluation of tiny branches and the residual neck.[42] However, we assumed that intraoperative diffusion-weighted imaging was useful to exclude acute ischemic complications.[22,23] Intraoperative MR imaging provided two advantages for STN-DBS.[6] One advantage was intraoperative visualization of the electrode location, as we were able to accurately locate the electrode by considering the reported artifact patterns.[36] The other advantage involved the higher signal/noise ratio during microelectrode recording due to the radiofrequency shielding. As techniques for directly imaging STN advance in the future, obtaining intraoperative MR images will become more important.[39] Spinal surgery may also be considered as an indication, as reported.[17]

The management of this system raises several issues. Maintenance of safety is very important.[11] To avoid magnetic absorption-related accidents, all staff working in the MR imaging-equipped operating

room must be educated concerning safety. The lines and ducts leading to the patient are potentially troublesome for patient transport, and continuous training is recommended. The limitation of surgical positioning is also important. Although we were able to perform complex approaches such as the anterior petrosal, lateral suboccipital, and transcondyle approaches, positioning limits must be considered. A flexible MR-compatible table that can be bent was recently reported,[18,19] and such improvements are necessary. The cost-benefit ratio must also be considered. The technology of the intraoperative MR imager has continuously progressed, and the importance of intraoperative images is often emphasized.[3,10,19,14] Further study is necessary to elucidate whether such a system improves patient outcomes over the long term. If such a system achieves social recognition, the health insurance system might be revised, and if healthcare providers adopt this technology widely, then further improvement of the cost-benefit ratio should result.

The integration of intraoperative high-field MR imaging and navigation is important for maximizing resection and minimizing complications in brain tumor surgeries, especially for infiltrative tumors such as gliomas. Tumors of the pituitary gland are also a good indication. Intraoperative imaging is not as advantageous for other extra-axial tumors, but still helpful in confirming the success of surgery or in deciding the volume and location of tumors to be intentionally left unresected. The system increases the accuracy and safety of surgery for cerebrovascular or functional diseases, but the indication is somewhat limited. The fully integrated system contributes to smooth workflow during surgery.

Acknowledgments

We would like to thank Mr. T. Nishihata (Department of Radiology, Nagoya Central Hospital) and Ms. H. Ishiguro (Department of Surgical Nursing, Nagoya Central Hospital) who have contributed since the installation, as well as all staff of Nagoya Central Hospital for their help in managing this system. We also thank Mr. Matthew Nielsen (Siemens, Healthcare Sector) for his technical advice regarding intraoperative MR imaging and for his help in the preparation of this manuscript.

References

1) Berman J, Berger MS, Mukherjee P, Henry RG: Diffusion-tensor imaging-guided tracking of fibers of the pyramidal tract combined with intraoperative cortical stimulation mapping in patients with gliomas. *J Neurosurg* 101: 66–72, 2004
2) Black PM, Moriarty T, Alexander E III, Stieg P, Woodard EJ, Gleason PL, Martin CH, Kikinis R, Schwartz RB, Jolesz FA: Development and implementation of intraoperative magnetic resonance imaging and its neurosurgical applications. *Neurosurgery* 41: 831–842, 1997
3) Bradley WG: Achieving gross total resection of brain tumors: intraoperative MR imaging can make a big difference. *AJNR Am J Neuroradiol* 23: 348–349, 2002
4) Calamante F, Ganesan V, Kirkham FJ, Jan W, Chong WK, Gadian DG, Connelly A: MR perfusion imaging in Moyamoya Syndrome: potential implications for clinical evaluation of occlusive cerebrovascular disease. *Stroke* 32: 2810–2816, 2001
5) Darakchiev BJ, Tew JM Jr, Bohinski RJ, Warnick RE: Adaptation of a standard low-field (0.3-T) system to the operating room: focus on pituitary adenomas. *Neurosurg Clin N Am* 16: 155–164, 2005
6) De Salles AA, Frighetto L, Behnke E, Sinha S, Tseng L, Torres R, Lee M, Cabatan-Awang C, Frysinger R: Functional neurosurgery in the MRI environment. *Minim Invasive Neurosurg* 47: 284–289, 2004
7) Fahlbusch R, Ganslandt O, Buchfelder M, Schott W, Nimsky C: Intraoperative magnetic resonance imaging during transsphenoidal surgery. *J Neurosurg* 95: 381–390, 2001
8) Fujimura M, Mugikura S, Shimizu H, Tominaga T: [Diagnostic value of perfusion-weighted MRI for evaluating postoperative alteration of cerebral hemodynamics following STA-MCA anastomosis in patients with moyamoya disease]. *No Shinkei Geka* 34: 801–809, 2006 (Jpn)
9) Gasser T, Ganslandt O, Sandalcioglu E, Stolke D, Fahlbusch R, Nimsky C: Intraoperative functional MRI: implementation and preliminary experience. *Neuroimage* 26: 685–693, 2005
10) Hall WA, Galichich W, Bergman T, Truwit CL: 3-Tesla intraoperative MR imaging for neurosurgery. *J Neurooncol* 77: 297–303, 2006
11) Hall WA, Liu H, Martin AJ, Pozza CH, Maxwell RE, Truwit CL: Safety, efficacy, and functionality of high-field strength interventional magnetic resonance imaging for neurosurgery. *Neurosurgery* 46: 632–641, 2000
12) Kamada K, Sawamura Y, Takeuchi F, Kawaguchi H, Kuriki S, Todo T, Masutani Y, Aoki S, Kirino T: Functional identification of the primary motor area by corticospinal tractography. *Neurosurgery* 56(1 Suppl): 98–109, 2005
13) Kamada K, Todo T, Masutani Y, Aoki S, Ino K, Takano T, Kirino T, Kawahara N, Morita A: Combined use of tractography-integrated functional neuronavigation and direct fiber stimulation. *J Neurosurg* 102: 664–672, 2005
14) Keles GE, Lundin DA, Lamborn KR, Chang EF, Ojemann G, Berger MS: Intraoperative subcortical stimulation mapping for hemispherical perirolandic gliomas located within or adjacent to the descending

motor pathways: evaluation of morbidity and assessment of functional outcome in 294 patients. *J Neurosurg* 100: 369–375, 2004
15) Lacroix M, Abi-Said D, Fourney DR, Gokaslan ZL, Shi W, DeMonte F, Lang FF, McCutcheon IE, Hassenbusch SJ, Holland E, Hess K, Michael C, Miller D, Sawaya R: A multivariate analysis of 416 patients with glioblastoma multiforme: prognosis, extent of resection, and survival. *J Neurosurg* 95: 190–198, 2001
16) Laws ER, Shaffrey ME, Morris A, Anderson FA Jr: Surgical management of intracranial gliomas — does radical resection improve outcome? *Acta Neurochir Suppl* 85: 47–53, 2003
17) Mastronardi L, Elsawaf A, Roperto R, Bozzao A, Caroli M, Ferrante M, Ferrante L: Prognostic relevance of the postoperative evolution of intramedullary spinal cord changes in signal intensity on magnetic resonance imaging after anterior decompression for cervical spondylotic myelopathy. *J Neurosurg Spine* 7: 615–622, 2007
18) Matsumae M, Fukuyama H, Ishikawa H, Osada T, Baba T, Mizokami Y, Atsumi H, Ishikawa H, Tsugu A, Tominaga J, Shiramizu H, Shimoda M: Fully functional MR-compatible flexible operating table resolves the neurosurgeon's dilemma over use of intraoperative MRI. *Tokai J Exp Clin Med* 33: 57–60, 2008
19) Matsumae M, Koizumi J, Fukuyama H, Ishikawa H, Mizokami Y, Baba T, Atsumi H, Tsugu A, Oda S, Tanaka Y, Osada T, Imai M, Ishiguro T, Yamamoto M, Tominaga T, Shimoda M, Imai Y: World's first magnetic resonance imaging/x-ray/operating room suite: a significant milestone in the improvement of neurosurgical diagnosis and treatment. *J Neurosurg* 107: 266–273, 2007
20) McKnight TR, Lamborn KR, Love TD, Berger MS, Chang S, Dillon WP, Bollen A, Nelson SJ: Correlation of magnetic resonance spectroscopic and growth characteristics within Grades II and III gliomas. *J Neurosurg* 106: 660–666, 2007
21) Mikuni N, Okada T, Enatsu R, Miki Y, Hanakawa T, Urayama S, Kikuta K, Takahashi JA, Nozaki K, Fukuyama H, Hashimoto N: Clinical impact of integrated functional neuronavigation and subcortical electrical stimulation to preserve motor function during resection of brain tumors. *J Neurosurg* 106: 593–598, 2007
22) Minematsu K, Li L, Fisher M, Sotak CH, Davis MA, Fiandaca MS: Diffusion-weighted magnetic resonance imaging: rapid and quantitative detection of focal brain ischemia. *Neurology* 42: 235–240, 1992
23) Moseley ME, Kucharczyk J, Mintorovitch J, Cohen Y, Kurhanewicz J, Derugin N, Asgari H, Norman D: Diffusion-weighted MR imaging of acute stroke: correlation with T2-weighted and magnetic susceptibility-enhanced MR imaging in cats. *AJNR Am J Neuroradiol* 11: 423–429, 1990
24) Muragaki Y, Iseki H, Maruyama T, Kawamata T, Yamane F, Nakamura R, Kubo O, Takakura K, Hori T: Usefulness of intraoperative magnetic resonance imaging for glioma surgery. *Acta Neurochir Suppl* 98: 67–75, 2006
25) Nimsky C, Fujita A, Ganslandt O, von Keller B, Fahlbush R: Volumetric assessment of glioma removal by intraoperative high-field magnetic resonance imaging. *Neurosurgery* 55: 358–370, 2004
26) Nimsky C, Fujita A, Ganslandt O, von Keller B, Kohmura E, Fahlbush R: Frameless stereotactic surgery using intraoperative high-field magnetic resonance imaging. *Neurol Med Chir (Tokyo)* 44: 522–533, 2004
27) Nimsky C, Ganslandt O, Buchfelder M, Fahlbusch R: Intraoperative visualization for resection of gliomas: the role of functional neuronavigation and intraoperative 1.5 T MRI. *Neurol Res* 28: 482–487, 2006
28) Nimsky C, Ganslandt O, Fahlbusch R: 1.5T: intraoperative imaging beyond standard anatomic imaging. *Neurosurg Clin N Am* 16: 185–200, vii, 2005
29) Nimsky C, Ganslandt O, Fahlbusch R: Implementation of fiber tract navigation. *Neurosurgery* 58(4 Suppl 2): ONS-292–304, 2006
30) Nimsky C, Ganslandt O, Hastreiter P, Wang R, Benner T, Sorensen AG, Fahlbusch R: Intraoperative diffusion-tensor MR imaging: shifting of white matter tracts during neurosurgical procedures — initial experience. *Radiology* 234: 218–225, 2005
31) Nimsky C, Ganslandt O, Hastreiter P, Wang R, Benner T, Sorensen AG, Fahlbusch R: Preoperative and intraoperative diffusion tensor imaging-based fiber tracking in glioma surgery. *Neurosurgery* 56: 130–137, 2005
32) Nimsky C, Ganslandt O, von Keller B, Fahlbush R: Intraoperative high-field-strength MR imaging: implementation and experience in 200 patients. *Radiology* 233: 67–78, 2004
33) Nimsky C, von Keller B, Ganslandt O, Fahlbusch R: Intraoperative high-field magnetic resonance imaging in transsphenoidal surgery of hormonally inactive pituitary macroadenomas. *Neurosurgery* 59: 105–114, 2006
34) Okada T, Mikuni N, Miki Y, Kikuta K, Urayama S, Hanakawa T, Fushimi Y, Yamamoto A, Kanagaki M, Fukuyama H, Hashimoto N, Togashi K: Corticospinal tract localization: integration of diffusion-tensor tractography at 3-T MR imaging with intraoperative white matter stimulation mapping — preliminary results. *Radiology* 240: 849–857, 2006
35) Ostergaard L, Sorensen AG, Kwong KK, Weisskoff RM, Gyldensted C, Rosen BR: High resolution measurement of cerebral blood flow using intravascular tracer bolus passages. Part II: Experimental comparison and preliminary results. *Magn Reson Med* 36: 726–736, 1996
36) Pollo C, Vingerhoets F, Pralong E, Ghika J, Maeder P, Meuli R, Thiran JP, Villemure JG: Localization of electrodes in the subthalamic nucleus on magnetic resonance imaging. *J Neurosurg* 106: 36–44, 2007
37) Rezai AR, Phillips M, Baker KB, Sharan AD, Nyen-

huis J, Tkach J, Henderson J, Shellock FG: Neurostimulation system used for deep brain stimulation (DBS): MR safety issues and implications of failing to follow safety recommendations. *Invest Radiol* 39: 300–303, 2004
38) Schneider JP, Trantakis C, Rubach M, Schulz T, Dietrich J, Winkler D, Renner C, Schober R, Geiger K, Brosteanu O, Zimmer C, Kahn T: Intraoperative MRI to guide the resection of primary supratentorial glioblastoma multiforme—a quantitative radiological analysis. *Neuroradiology* 47: 489–500, 2005
39) Slavin KV, Thulborn KR, Wess C, Nersesyan H: Direct visualization of the human subthalamic nucleus with 3T MR imaging. *AJNR Am J Neuroradiol* 27: 80–84, 2006
40) Steinmeier R, Fahlbusch R, Ganslandt O, Nimsky C, Buchfelder M, Kaus M, Heigi T, Lenz G, Kuth R, Huk W: Intraoperative magnetic resonance imaging with the magnetom open scanner: concepts, neurosurgical indications, and procedures: a preliminary report. *Neurosurgery* 43: 739–747, 1998
41) Sutherland GR, Kaibara T, Louw D, Hoult DI, Tomanek B, Sanders J: A mobile high-field magnetic resonance system for neurosurgery. *J Neurosurg* 91: 804–813, 1999
42) Sutherland GR, Kaibara T, Wallace C, Tomanek B, Richter M: Intraoperative assessment of aneurysm clipping using magnetic resonance angiography and diffusion-weighted imaging: technical case report. *Neurosurgery* 50: 893–898, 2002
43) Suzuki Y, Nogoro M, Shibuya M, Yoshida J, Noguro T, Watanabe K: Surgical treatment for pediatric moyamoya disease: Use of the superficial temporal artery for both areas supplied by the anterior and middle cerebral arteries. *Neurosurgery* 40: 324–330, 1997
44) Truwit CL, Hall WA: Intraoperative magnetic resonance imaging-guided neurosurgery at 3-T. *Neurosurgery* 58(4 Suppl 2): ONS-338–ONS-346, 2006
45) Wityk RJ, Hillis A, Beauchamp N, Barker PB, Rigamonti D: Perfusion-weighted magnetic resonance imaging in adult moyamoya syndrome: characteristic patterns and change after surgical intervention: case report. *Neurosurgery* 51: 1499–1505, 2002

Address reprint requests to: Satoshi Maesawa, M.D., Department of Neurosurgery, Nagoya University Graduate School of Medicine, 65 Tsurumai-cho, Showa-ku, Nagoya, Aichi 466-8550, Japan.
e-mail: smaesawa@med.nagoya-u.ac.jp

Commentary

This paper reports on the excellent experience of the authors using intraoperative high field MRI and neuronavigation. All possible applications have been tested and critically reviewed, from glioma surgery, to cerebrovascular procedures, to functional neurosurgery. The conclusion is that the main utility of intraoperative MRI is to solve problems connected with tumor removal: in particular, to ascertain gross total removal of the lesion, and to spare functionally relevant subcortical white matter tracts, such as pyramidal tract, optic pathways and speech related tracts. Very honestly, the authors point out the limitation of this procedure as well: for instance, the difficulties in demonstrating patency of perforators, or sack residuals, in aneurysm surgery, due to the artifacts of the metallic clip that obscure the vision of the surrounding region. Moreover, they suggest that the best results for neurooncology, in term of radical surgery with respect of normal functioning structures, is achieved by the coupling of intraoperative MRI with other monitoring systems, particularly neuronavigation, but also neurophysiological intraoperative testing. Finally, they mention the financial aspect, that in these days is not the least important. It would be nice to organize a prospective work to compare the cost/effect of two different methods to obtain the above mentioned results in glioma surgery (radicality and respect of normal tracts), namely intraoperative MRI and 5-ALA fluorescence, both integrated with neurophysiological monitoring. I do think that the anatomical check (namely MRI) will be at the end superior, but still there is a possible role also for different, less costly, procedures.

Alessandro Ducati, *M.D.*
Ordinario di Neurochirurgia
Universita' di Torino
Torino, Italy

The authors did meaningful and interesting work to provide the initial experiences of high-field 1.5T intraoperative magnetic resonance imaging (iMRI) and neuro-navigation in 100 cases of neurosurgical procedures and to explore its clinical indications and limitations.

The intraoperative imaging is an important tool in modern minimally invasive neurosurgery, and serves to maximize lesion removal and minimize morbidity. The best use of iMRI is for the lesions without identifiable boundaries, located in eloquent areas, deep-seated, and difficult to find and access. Its use can be exemplified in glioma surgery. As we all know, the principle of the glioma surgery is maximal safe tumor resection, however, to realize this aim remains a

challenge to all neurosurgeons. Without intraoperative image guidance, tumor resection, to a high extent, depends on surgeons' experience. Often, the degree of tumor resection is prone to be overestimated and the potential risk of neurological deficit is increased by pursuing greater resection. I agree that glioma surgery is a good indication for iMRI and neuro-navigation.

iMRI and neuro-navigation helps to localize lesion, identify vital neurovascular structures, and detect remnant tumor. However, every coin has two sides, this system is not completely reliable. It is always essential that surgeons must make right and timely judgements intraoperatively. Besides, the high cost limits its wide application. There is less value for tumors with clear margins according to the cost-effectiveness principle. Maybe we can get more benefit from the multimodality use of more techniques, such as the fluoroscope in glioma surgery and intraoperative fluorescein angiography in surgery of cerebrovascular diseases.

Safety and effectiveness is the final goal of surgery. iMRI and neuro-navigation can further this aim, and the authors have provided a meaningful study and obtained good results which has important value in image-guided neurosurgery.

Dapeng MO, M.D.
and Shengde BAO, M.D.
Department of Neurosurgery
Peking University First Hospital
Beijing, P.R.C.